

# Circulation of hydraulically ponded turbidity currents in three-dimensional minibasins with implications for turbidite shape

John Kevin Reece<sup>1</sup>, Kyle Martin Straub<sup>1</sup>, and Robert Michael Dorrell<sup>2</sup>

<sup>1</sup>Tulane University

<sup>2</sup>University of Hull

August 4, 2023

## Abstract

Minibasins on continental margins trap turbidity currents transporting material downslope, but little is known about the inherently three-dimensional (3-D) mechanics of these confined flows. Utilizing new methodology, experimental results quantify flow dynamics in minibasins for the first time. It is shown that dynamics are dominated by 3-D circulation cell structures, across the fill-to-strip-to-spill transition that are controlled by flow discharge. Measurements of velocity throughout circulation cells indicate vorticity dominates strain rate with fluid rotating into the center of cells where it upwells: this influences minibasin sediment trapping potential and deposit heterogeneity. Flow properties link to depositional patterns on minibasin slopes. Specifically, higher input discharges are correlated with higher fluxes into the center of minibasins and reduced deposit tapering on minibasin slopes. This geometry is linked to the amount of sediment rich flow runup on the distal minibasin wall, where flow and sediment is delivered to circulation cells.

## Hosted file

970167\_0\_art\_file\_11237285\_ryxsdv.docx available at <https://authorea.com/users/645013/articles/657653-circulation-of-hydraulically-ponded-turbidity-currents-in-three-dimensional-minibasins-with-implications-for-turbidite-shape>

## Hosted file

970167\_0\_supp\_11237288\_rymsdv.docx available at <https://authorea.com/users/645013/articles/657653-circulation-of-hydraulically-ponded-turbidity-currents-in-three-dimensional-minibasins-with-implications-for-turbidite-shape>

## Hosted file

970167\_0\_supp\_11237311\_ryqstn.docx available at <https://authorea.com/users/645013/articles/657653-circulation-of-hydraulically-ponded-turbidity-currents-in-three-dimensional-minibasins-with-implications-for-turbidite-shape>

1 **Circulation of hydraulically ponded turbidity currents in three-dimensional minibasins with**  
2 **implications for turbidite shape**

3

4 J. Kevin Reece<sup>1</sup>, Robert M. Dorrell<sup>2</sup>, & Kyle M. Straub<sup>1</sup>

5

6 <sup>1</sup>Department of Earth and Environmental Sciences, Tulane University, New Orleans, LA 70118, U.S.A.

7 <sup>2</sup>Energy and Environment Institute, University of Hull, Hull, HU6 7RX, United Kingdom

8

9 Correspondence to: J. Kevin Reece (jreece@tulane.edu)

10

11 **Abstract**

12 Minibasins on continental margins trap turbidity currents transporting material downslope, but  
13 little is known about the inherently three-dimensional (3-D) mechanics of these confined flows. Utilizing  
14 new methodology, experimental results quantify flow dynamics in minibasins for the first time. It is  
15 shown that dynamics are dominated by 3-D circulation cell structures, across the fill-to-strip-to-spill  
16 transition that are controlled by flow discharge. Measurements of velocity throughout circulation cells  
17 indicate vorticity dominates strain rate with fluid rotating into the center of cells where it upwells: this  
18 influences minibasin sediment trapping potential and deposit heterogeneity. Flow properties link to  
19 depositional patterns on minibasin slopes. Specifically, higher input discharges are correlated with higher  
20 fluxes into the center of minibasins and reduced deposit tapering on minibasin slopes. This geometry is  
21 linked to the amount of sediment rich flow runup on the distal minibasin wall, where flow and sediment is  
22 delivered to circulation cells.

23

## 24 **Introduction**

25           Turbidity currents, a class of gravity flows that gain excess density by suspension of sediment,  
26 are the primary particulate transport process on the slope of continental margins [Talling *et al.*, 2015].  
27 These flows represent geohazards to submarine infrastructure, while also transporting particulate organic  
28 carbon and microplastics to deep marine reservoirs [Carter *et al.*, 2014; Hage *et al.*, 2020; Pohl *et al.*,  
29 2020b; Sparkes *et al.*, 2015]. On many margins, turbidity currents encounter topographic obstacles  
30 including local depressions, seamounts, and shale ridges [Nasr-Azadani & Meiburg, 2014; Straub &  
31 Mohrig, 2009; Völker *et al.*, 2008]. Depressions large enough to impact deposition from turbidity currents  
32 are often termed minibasins [Mitchum Jr *et al.*, 1977]. Their ability to slow the progression of turbidity  
33 currents and sometimes hydraulically pond flows makes them hotspots for clastic sediment, particulate  
34 organic carbon, and microplastic accumulation [Dorrell *et al.*, 2018; Lamb *et al.*, 2004; Pirmez *et al.*,  
35 2012; Prather *et al.*, 2012].

36           There is a lack of direct observations of field scale turbidity currents interacting with minibasins,  
37 primarily due to their: 1) relatively inaccessible locations, 2) unpredictable flow occurrences, and 3) high  
38 flow shear stresses that can destroy equipment [Azpiroz-Zabala *et al.*, 2017; Khripounoff *et al.*, 2003].  
39 Development of theory has thus leveraged numerical and physical experiments [Bastianon *et al.*, 2021;  
40 Brunt *et al.*, 2004; Toniolo *et al.*, 2006b; Traer *et al.*, 2018; Violet *et al.*, 2005; Wang *et al.*, 2017].  
41 However, due to computational demands, many numerical models utilize depth average flow parameters,  
42 limiting their applicability in settings where vertical flow properties vary strongly in space and time, such  
43 as in minibasins [Meiburg *et al.*, 2015; Yang *et al.*, 2019]. In addition, while a few physical experiments  
44 document flow interactions with topography in three-dimensions, 3-D, [Maharaj, 2012; Soutter *et al.*,  
45 2021; Violet *et al.*, 2005], most physical experiments on turbidity current – minibasin interactions have  
46 been conducted in 2-D [Lamb *et al.*, 2004; Patacci *et al.*, 2015; Pohl *et al.*, 2020a; Spinewine *et al.*, 2009;  
47 Toniolo *et al.*, 2006b]. Ponding occurs due to a topographic obstacle, which triggers a rapid spatial flow  
48 deceleration to extremely low densimetric Froude conditions and the formation of a placid flow transition  
49 with the overlying ambient fluid, decreasing the entrainment of ambient fluid into the current [Lamb *et*

50 *al.*, 2004; van Andel and Komar, 1969]. In 2-D (Fig. 1A), ponding produces concentration profiles with  
51 little vertical structure, as sediment lost to deposition is replaced from above with more sediment laden  
52 flow. This produces tabular deposits that do not rapidly thin against confining topography [Lamb *et al.*,  
53 2004; Toniolo *et al.*, 2006b]. Flow circulation within 2-D minibasins was documented along a vertical  
54 plane, with a return flow positioned above down-basin directed flow [Patacci *et al.*, 2015]. It is unclear if  
55 this style of circulation develops in 3-D minibasins.

56 We explore the influence of flow discharge into minibasins on the 3-D velocity field, structure of  
57 sediment concentration profiles, and turbidite shape. Flow discharge is adjusted by changing flow width,  
58 keeping all other input conditions constant. The setup is designed to capture endmembers across a  
59 minibasin fill-to-strip-to-spill transition [Badalini *et al.*, 2000; Beaubouef and Abreu, 2006; Beaubouef  
60 and Friedmann, 2000; Satterfield and Behrens, 1990; Winker, 1996]. The campaign quantifies lateral  
61 circulation cells, which we link to upwelling flow that could impact sedimentation processes by  
62 countering the still fluid settling velocity of particles.

63

## 64 **Experimental Design**

65 Experiments were performed in a 6 x 4 x 2.2 m basin with an inner floor, surrounded by moats.  
66 Circular minibasins were carved into 300  $\mu\text{m}$  sand with a diameter of 3 m, 10% sidewall slopes, and a  
67 0.12 m depth. Dimensionless ratios characterizing minibasin topography, including side wall slopes, fall  
68 within distributions generated from 2,324 depressions extracted from the Bureau of Ocean and Energy  
69 Management's bathymetric dataset of the northern Gulf of Mexico [BOEM, 2017]. Minibasins were  
70 submerged in fresh water with 0.69 m of water above the minibasin rim. Sustained turbidity currents were  
71 delivered to the rim of minibasins for 30 minutes. Input flows had densimetric Froude numbers of 1.1,  
72 were 48 mm thick, and had an excess density of 2.9%.

73 Our experiments utilized a novel aluminum oxide sediment (particle density of 3950  $\text{kg}/\text{m}^3$ ) of  
74 low cohesivity due to a deflocculant mixture containing calcium carbonate and sodium  
75 hexametaphosphate (SHMP) that was used to inhibit particle amalgamation. Volumetric sediment

76 concentration was 1% with  $D_5$ ,  $D_{25}$ ,  $D_{50}$ ,  $D_{75}$ ,  $D_{95}$  of 6, 11, 14, 17, and 24  $\mu\text{m}$ , respectively. The high-  
77 density aluminum oxide sediment produces significant excess density from low volumetric sediment  
78 concentrations, generating swifter, more turbulent flows [Fukuda et al., 2023]. This allows transport of  
79 particles to greater distances prior to deposition, relative to experimental flows comprised of quartz  
80 sediment.

81 Three experiments were performed, each composed of two flow events, and are referred to as the  
82 low-flux (24 l/min & 65 mm entrance width), mid-flux (47.7 l/min & 130 mm width), and high-flux (96.9  
83 l/min & 260 mm width) experiments. During the first event a 30 min long 3-component velocity profile  
84 timeseries was collected at minibasin center using a Pulse Coherent Acoustic Doppler Profiler (PCADP),  
85 in addition to equilibrium sediment concentration profiles collected 26 – 27.5 min into the flows. During  
86 the second event, velocity profiles were collected after equilibrium conditions were reached at a set of  
87 positions covering the river-left side of the minibasins. Topography was mapped with a displacement  
88 laser before and after each experiment.

89

## 90 **Results**

91

### 92 *Minibasin center conditions*

93 Equilibrium velocity conditions at minibasin center are estimated by averaging profiles collected  
94 from the first flow of each experiment over the duration that concentration profiles were collected. Here,  
95  $u$ ,  $v$ , and  $w$  refer to the velocity components in the down-basin, cross-basin, and vertical directions,  
96 respectively. For comparison,  $u$  velocity profiles at minibasin center are normalized by the maximum  
97 velocity of a profile,  $u_{max}$  (Fig. 2A). The low-flux condition has the most complicated velocity structure,  
98 with low velocities in the lower third of the flow, peak velocities in the middle third and a rapid velocity  
99 reduction in the upper third of the flow. The mid and high-flux conditions are less stratified and have peak  
100 velocities just below the minibasin rim elevation.

101 Sediment concentration profiles are compared following normalization by near bed conditions,  
102  $C_{nb}$  (Fig. 2B). The low-flux experiment, which was the most contained within the minibasin, is the most  
103 stratified. The mid and high-flux conditions are well mixed in the lower two-thirds of the elevations  
104 contained within the minibasin. Sediment concentrations then rapidly decrease to near zero values  
105 approaching the rim elevation.

106

### 107 *Evolution of down minibasin velocity*

108 Experiments had differences in discharge, controlled by initial flow width, that generated  
109 different minibasin floor velocity due to varying lateral flow expansion (Fig. 2C) between experiments.  
110 All experiments show a rapid spatial deceleration in  $u_{max}$  with distance into the minibasin, as flow  
111 ponding triggered a rapid increase in flow height and decrease in densimetric Froude number. Minibasin  
112 floor velocities are used to estimate flow runup onto the distal minibasin wall. The magnitude of runup is  
113 estimated by:

$$114 \Delta z = \frac{\rho_c u_{max}^2}{(\rho_c - \rho_a) 2g} \quad [EQ. 1]$$

115 where  $\rho_c$  and  $\rho_a$  are current and ambient fluid densities and  $g$  is gravitational acceleration [Dorrell et al.,  
116 2018; Straub et al., 2008]. Here,  $\rho_c$  is estimated from measurements of sediment concentration. Use of  
117 Eq. 1 results in estimates of 3.9, 9.5, and 27.8 mm of runup for the low, mid, and high flux experiments,  
118 respectively. Finally, we note that measurements of  $u_{max}$  above the downstream minibasin rim indicate  
119 that the experiments captured the fill-to-strip-to-spill transition. The low-flux experiment (characterizing  
120 the “fill” endmember) has near zero  $u_{max}$  above the distal rim, which ticks up to ~0.015 m/s for the mid-  
121 flux (“strip”) condition and reaches ~0.035 m/s for the high-flux (“spill”) condition.

122

### 123 *Circulation Cells*

124 Overhead imagery (Mov. S1-3) and velocity measurements covering the river left hand side of  
125 the minibasins (Figs. 3&4) capture fluid circulation cells spawned from the current interaction with the

126 distal slope. We characterize fluid movement through minibasins using vector maps of the temporally  
127 averaged depth integrated fluid flux in the down and cross basin directions:

$$128 \quad q_u = \int_0^H u dz \quad [EQ. 2A]$$

$$129 \quad q_v = \int_0^H v dz \quad [EQ. 2B]$$

130 where  $H$  represents the current height, estimated with the integral length scale [Ellison and Turner, 1959]  
131 (Fig. 3A). Temporal averaging was done over the duration that the PCADP sampled each site. When  
132 vectors are scaled by input discharge, the structure of the discharge field is similar across experiments.  
133 High fluxes down the proximal slope efficiently deliver fluid and sediment to the center of minibasins.  
134 Down basin depth integrated fluxes then rapidly decrease going up the distal minibasin slope as fluid is  
135 routed into circulation cells. Due to the inlet flow entering the center of the basin in these experiments, the  
136 cells are laterally offset and positioned over the lower lateral slope.

137 Gradients in the velocity field of the flow adjusting to the confining minibasin describe local fluid  
138 stretching (strain) and rotation (vorticity). We quantify and compare the vorticity and strain rate at all  
139 sample points. From Dubief and Delcayre, 2000, the horizontal strain rate tensor is calculated from the  
140 symmetric part of the velocity gradient tensor as:

$$141 \quad S = \frac{1}{2}[(\delta u / \delta x) + (\delta v / \delta y)] \quad [EQ. 3]$$

142 and the horizontal vorticity is calculated from the asymmetric part of the velocity gradient tensor as:

$$143 \quad \Omega = \frac{1}{2}[(\delta v / \delta x) - (\delta u / \delta y)] \quad [EQ. 4]$$

144 where  $x$  and  $y$  are down and cross basin locations, respectively. We quantify and visualize strength  
145 of rotation relative to the lateral strain rate of the fluid using the Q-criterion,  $Q$ :

146

147 Positive  $Q$  indicates vorticity exceeds shear (strain rate tensor), and negative values represent areas where  
148 strain rate dominates the 3-D flow field [Dubief and Delcayre, 2000]. We hypothesize that circulation  
149 with positive  $Q$  at the cell center is associated with upwelling fluid, a consequence of fluid mass

150 conservation. This 3-D flow pattern would control sediment transport and deposition. Maps of  $Q$  at  
151 various minibasin depths highlight that the center of the circulation cell has vorticity that exceeds the  
152 strain rate (Fig. 3D-E). Here, we present results from the high-flux condition, which are similar in  
153 structure (but different in magnitude) to the other experiments. The center of the cell migrates laterally  
154 away from minibasin center with increasing minibasin height. While  $Q$  values indicate whether vorticity  
155 or strain rate is larger at a point, it does not inform on the fractional difference of the two. This can be  
156 estimated with the kinematic vorticity number [Dubief and Delcayre, 2000]:

$$157 \quad \Omega_k^* = \frac{||\Omega||}{||S||} \quad [EQ. 6]$$

158 We track vorticity, strain rate, and the  $w$  velocity component near the center of the circulation cell for all  
159 heights in the minibasin. The center of this cell laterally migrates away from minibasin center with  
160 increasing water depth. Near the center of the vortex,  $\Omega_k^*$  is between 2 to 75, suggesting limited fluid  
161 stretching during rotation (Fig. 3B). This is associated with a profile of the  $w$  velocity component with  
162 upwards directed flow that considerably exceeds the still sediment fall velocity,  $w_s$ , of the median grain  
163 size introduced to the basin (0.5 mm/s) and the vertical detrainment velocity (Fig. 3C). This upwelling  
164 flow will influence sediment settling velocities as a function of the grain size distribution, leading to  
165 enhanced trapping potential of coarse, relative to fine, particles. However, the profile has considerable  
166 structure with significant upwards directed flow in the lower third of the current, that reduces to near zero  
167 in the middle of the flow. This reduction might be linked to low vertical shear at the  $u_{max}$  elevation [Islam  
168 and Imran, 2010]. The top third of the flow again is defined by upwelling flow that exceeds  $w_s$ .

169 We use velocity measurements to calculate flow streamlines. The streamlines capture horizontal  
170 gathering of flow into the center of the circulation cells and strong upwelling flow at the cell center (Fig.  
171 4).

172

173 ***Minibasin margin onlap***

174 Sedimentation patterns are characterized using isopach maps, calculated by differencing initial  
175 and final topography for an experiment. As a different total volume of sediment was released into the  
176 basin for each experiment, due to different flow discharges, we normalized deposition by the mean  
177 deposit thickness over the flat minibasins floor,  $D^*$  (Fig. 5A-C). While the structure of the concentration  
178 profiles at minibasin center might suggest similar gradients in deposition with distance up minibasin  
179 slopes, we observe stark differences between experiments in the deposit taper against slopes. Most of the  
180 sediment released into the low-flux experiment is contained within the minibasin, with deposit thickness  
181 at the minibasin rim only 10% of minibasin center thickness. In contrast, deposit thickness at the rim  
182 elevation exceeds 50% of minibasin center thickness for the high-flux experiment, highlighting the  
183 spilling nature of this experiment. Excluding data from the proximal slope, we quantify the rate of  
184 thinning up minibasin slopes by binning measurements of normalized deposit thickness by elevation  
185 above minibasin center, with 1 mm tall bins. Bin averaged data generate an average onlapping profile that  
186 is a function of normalized minibasin elevation, equal to elevation above minibasin center / minibasin  
187 depth,  $z^*$  (Fig. 5D). We use these profiles to calculate an onlap index, equal to the area underneath the  
188 curves in figure 5D:

$$189 \quad I_o = \int_0^1 D^* dz^* \quad [EQ. 7]$$

190 Thus, sedimentation that does not change thickness up minibasin walls would yield an  $I_o$  of 1, while a  
191 linear decrease in sedimentation from minibasin center values to zero deposition on the minibasin rim  
192 would yield an  $I_o$  of 0.5. We measure  $I_o$  values of 0.48, 0.58, and 0.72 for the low, mid, and high flux  
193 experiments, respectively.

194

## 195 Discussion

196 A key finding of this study is the new observation of paired circulation cells resulting from  
197 turbidity currents interacting with minibasin topography (Mov. S1-3, Fig. 1B & 3-4). Velocities within  
198 these circulation cells vary as a function of input discharge. However, their structure, following

199 normalization, is remarkably similar over the fill-to-strip-to-spill spectrum (Fig. 3A). This structure is  
200 setup during the initial traverse of the turbidity current front, which does not fill the full minibasin width  
201 (Mov. S1-3). Reflection off the distal slope results in return flow along lateral minibasin slopes. This  
202 same structure is observed during equilibrium conditions, where inlet flow sends dye into the minibasin  
203 center with minimal widening until it reflects laterally when running up the distal slope (Mov. S1-3).

204 Prior 2-D experiments highlighted circulation in minibasins along a vertical plane (Fig. 1A)  
205 [Patacci *et al.*, 2015]. During equilibrium conditions, we do not observe return flow at the center of the  
206 minibasin in the experiments reported here (Fig. 2). This suggests the ability of currents to laterally  
207 expand and setup circulation along a horizontal plane suppresses the development of circulation along a  
208 vertical plane. As a result, sediment charged flow that cannot escape over the distal rim is directed to and  
209 deposited on the lateral slopes.

210 Study of circulation cells in flows has a long history in sedimentology, including controlling the  
211 formation of river meanders [Einstein, 1926] and bedform development [Gilbert, 1914]. Here, the centers  
212 of minibasin circulation cells have positive Q-criterion indicating the importance of fluid rotation in  
213 ponded turbidity currents. The gathering of flow towards the center of cells (Fig. 4) drives upwelling with  
214 vertical fluid velocities that exceed the still fluid settling velocity of sediment introduced to the  
215 minibasins (Figs. 3C&4). However, vertical velocity profiles suggest sediment entering the lower portions  
216 of the vortex might not be able to transit to the flow top. This likely creates a sediment trap that enhances  
217 sediment concentrations until the flow wanes and sediment rains to the bed. This could be the reason for  
218 the thick deposits offset either side of minibasin center in the high-flux experiment (Fig. 5C). However,  
219 sediment entering the vortex in the upper third of the flow likely can escape the flow top, reducing basin  
220 sediment trapping potential relative to theory generated from 2-D minibasin experiments [Lamb *et al.*,  
221 2006]. Unfortunately, we do not have information on deposit particle sizes throughout the minibasin.  
222 However, we propose that circulation cells play a significant role in the fractionation of particulates,  
223 pollutants, and nutrients.

224 Deflection of flow running up the distal slope routes sediment laden flow over the lateral  
225 minibasin slopes, resulting in deposition throughout the minibasin (Fig. 1B). We highlight that sediment  
226 concentration profiles at minibasin center are similar for the three experimental conditions, but the onlap  
227 index,  $I_o$ , varies greatly between experiments (Fig. 5). We link this to varying degrees of flow runup onto  
228 distal minibasin slopes. We compare  $\Delta z$  resulting from runup to our onlap index and note a near linear  
229 trend (Fig. 5E). This supports that the degree of runup on the distal minibasin slope influences the amount  
230 of sediment delivered to circulation cells that then distribute sediment minibasin wide.

231 Finally, we note that the vertical flow structure captured in these experiments differs strongly  
232 from unconfined turbidity currents [Altinakar et al., 1996; Sequeiros et al., 2010]. Development of rules  
233 and theory emanating from 3-D experiments will aid future development of layer averaged models of  
234 turbidity currents interacting with complicated topography.

235

## 236 **Conclusions and implications**

237 As some of the largest sediment transport processes on the Earth surface, turbidity currents are  
238 critically important. Traversing the seafloor they are often subject to large topographic constraints, such  
239 as minibasins. Here new experimental methodology is developed and used to study the dynamics of  
240 turbidity currents as they interact as with three dimensional minibasin topography.

241 For the first time it is shown that three-dimensional flow structure generates inwards spiraling  
242 horizontal flow circulation cells, with strong central upwelling jets (Fig. 1B). Fluid rotation in these cells  
243 is significant, with vorticity exceeding the fluid's strain rate. Mass conservation at the center of  
244 circulation cells drives the upwelling. However, a dead zone of low vertical velocity separates regions  
245 where the velocity of upwelling fluid significantly exceeds the still fluid sediment fall velocity.

246 The dynamics presented here will both distribute and fractionate particulates, pollutants and  
247 nutrients transported by turbidity currents. Specifically, the ability for minibasins to act as a sink for  
248 microplastics and particulate organic carbon, which have low settling velocities, may be significantly  
249 reduced.

250  
251  
252  
253  
254  
255  
256  
257  
258  
259  
260  
261  
262  
263  
264  
265  
266  
267  
268  
269  
270  
271  
272  
273  
274

**Acknowledgements**

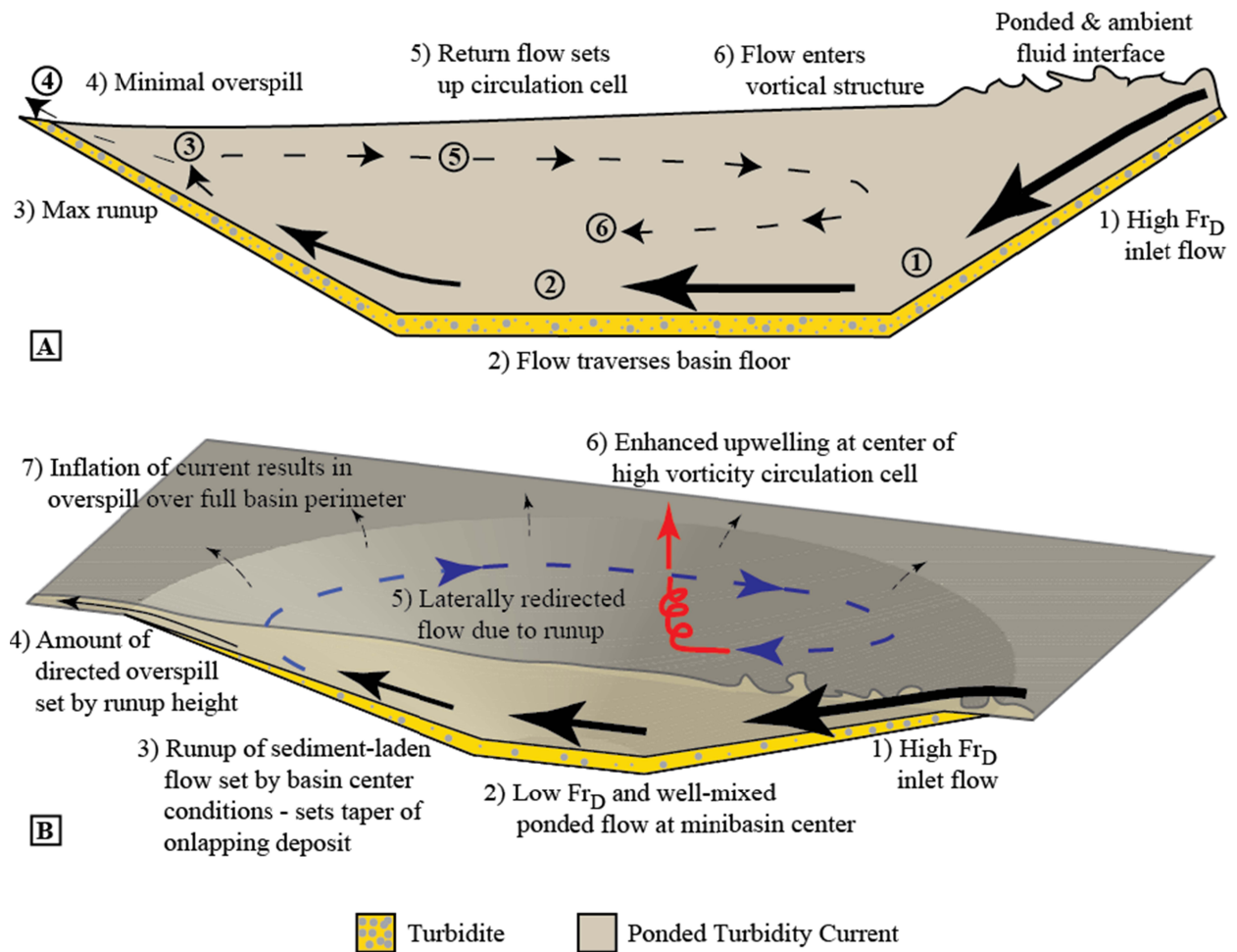
Support from grants to Reece from The Geological Society of America, American Association of Petroleum Geology, and by SEPM, Society for Sedimentary Geology; grants to Straub from The Tulane Carol Lavin Bernick Fund, ExxonMobil, The U.S. - Israel Energy Center funded through the Binational Industry Research and Development Foundation; and grants to Dorrell by the UK Natural Environment Research Council NE/S014535/1.

**Data availability statement**

Data that support this study can be downloaded at <https://doi.org/10.5281/zenodo.8144554>.

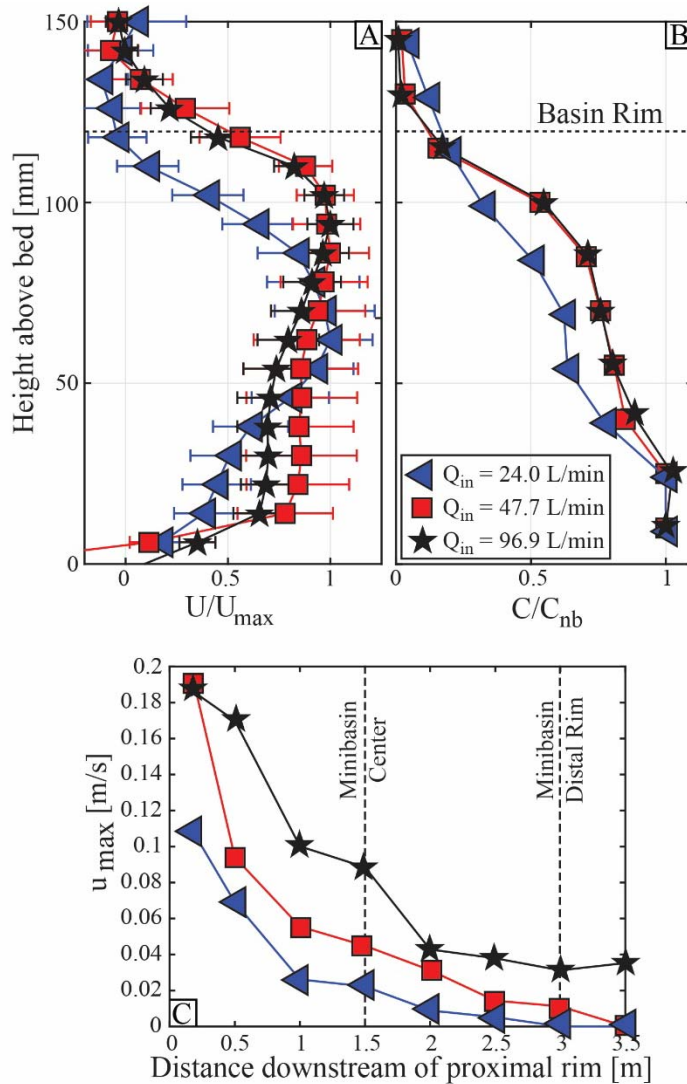
275  
 276  
 277  
 278  
 279  
 280

**Figures**



281  
 282  
 283  
 284  
 285

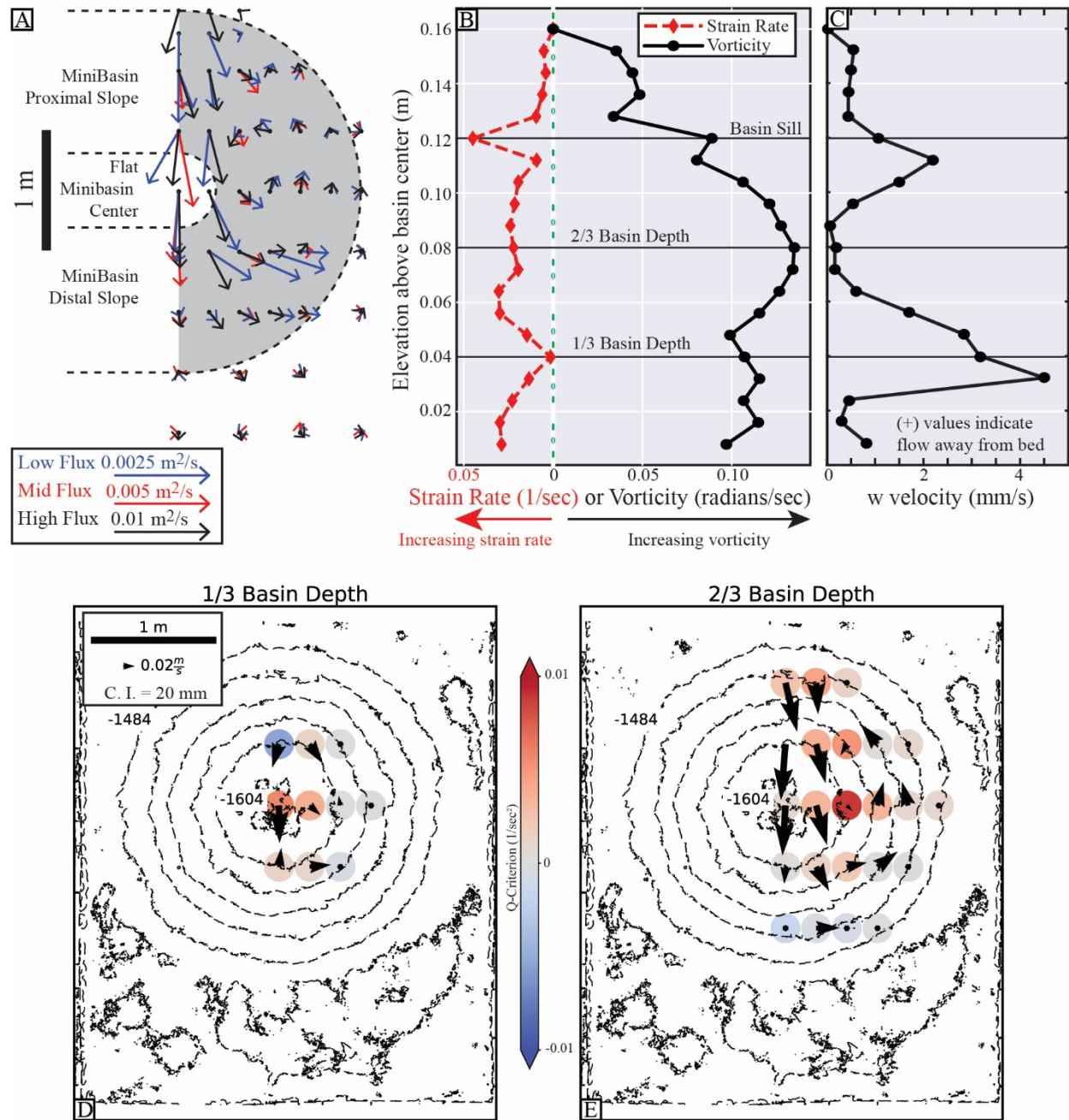
**Figure 1.** A) 2-D and B) 3-D schematics of circulation cell development inside topographically enclosed minibasins.



287

288

289 **Figure 2.** Velocity and concentration measurements at minibasin center and flow evolution along the  
 290 down basin traverse. A-B) Profiles at minibasin center normalized by the maximum velocity in a profile  
 291 and near bed sediment concentration, respectively. C) Measurements of the maximum velocity along the  
 292 basin bisect line.

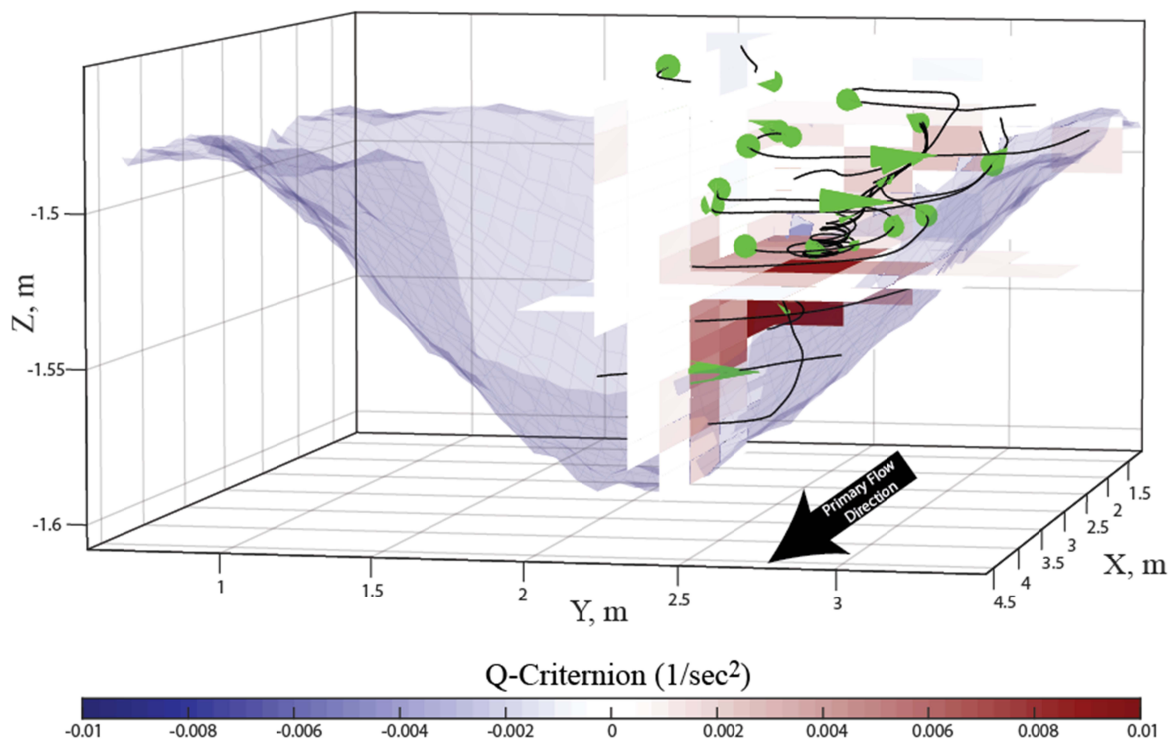


293

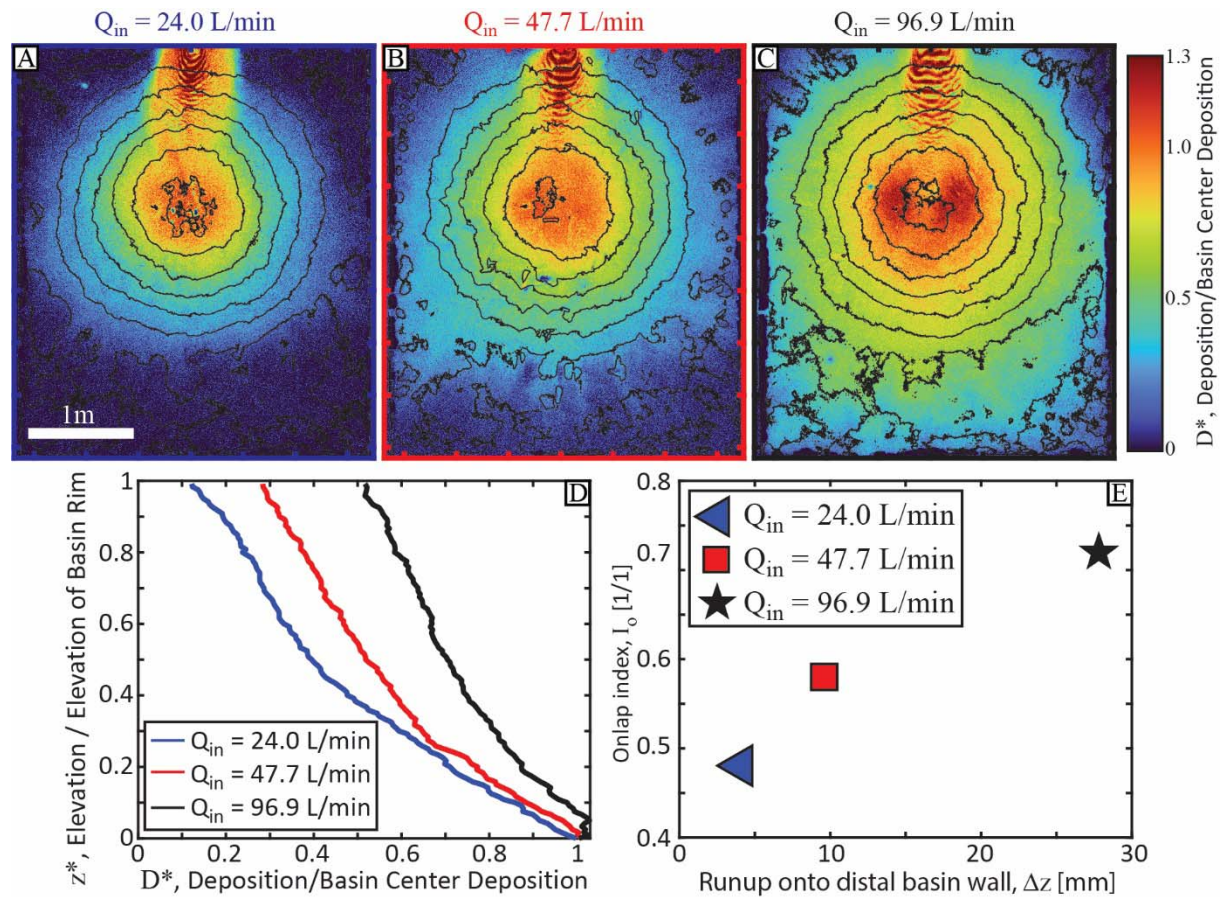
294

295 **Figure 3.** Characterization of minibasin three-dimensional velocity field. Primary flow direction in maps  
 296 is from top to bottom. A) Vector field of the depth integrated fluid flux. B) Magnitude of flow strain rate  
 297 and vorticity and C)  $w$  component of velocity as a function of elevation above floor of minibasin and  
 298 lateral position following center of circulation cell, which migrates away from basin center with  
 299 increasing flow height, as defined by the maximum Q-criterion. C-D) Measurements of Q-criterion

300 (colored dots) for the high-flux experiment along depth slices. Quivers show the  $u$  and  $v$  velocity  
301 components on each depth slice. Contours represent pre-flow topography.



302  
303  
304 **Figure 4.** 3-D streamline and cone plots detailing flow structure in the high-flux experiment. Minibasin  
305 topography pre-flow is illustrated in semitransparent blue mesh, with distal basin topography excluded to  
306 aid visualization. 10x Vertical exaggeration applied to aid visualization. Horizontal and vertical slices  
307 display Q-criterion. Note upwelling and spiraling current at center of circulation that corresponds to the  
308 maximum Q-criterion values.  
309



310

311

312 **Figure 5.** Measurements of sediment deposition and link to the turbidity current velocity field. A-C)

313 Sediment isopach maps normalized by minibasin center conditions. Contours represent initial minibasin

314 topography. Primary flow direction in all maps is from top to bottom. D) average sediment deposition

315 profile up minibasin slopes. E) Cross-plot of estimated distal minibasin wall flow runup to onlap index.

316

317

318

319

320

321

322

323 **References**

- 324 Altinakar, M. S., W. H. Graf, and E. J. Hopfinger (1996), Flow structure in turbidity currents,  
325 *Journal of Hydraulic Research*, 34, 713-718.
- 326 Azpiroz-Zabala, M., M. J. Cartigny, P. J. Talling, D. R. Parsons, E. J. Sumner, M. A. Clare, S. M.  
327 Simmons, C. Cooper, and E. L. Pope (2017), Newly recognized turbidity current structure can  
328 explain prolonged flushing of submarine canyons, *Science advances*, 3(10), e1700200.
- 329 Badalini, G., B. Kneller, and C. D. Winker (2000), Architecture and Processes in the Late  
330 Pleistocene Brazos-Trinity Turbidite System, Gulf of Mexico Continental Slope, *GCSSEPM, 20th*  
331 *Annual Research Conference Deep-Water Reservoirs of the World*, 16-34.
- 332 Bastianon, E., E. Viparelli, A. Cantelli, and J. Imran (2021), 2D numerical simulation of the filling  
333 process of submarine minibasins: Study of deposit architecture, *Journal of Sedimentary*  
334 *Research*, 91(4), 399-414.
- 335 Beaubouef, R., and V. Abreu (2006), Basin 4 of the Brazos-Trinity slope system: Anatomy of the  
336 terminal portion of an intra-slope lowstand systems tract.
- 337 Beaubouef, R., and S. Friedmann (2000), High resolution seismic/sequence stratigraphic  
338 framework for the evolution of Pleistocene intra slope basins, western Gulf of Mexico:  
339 depositional models and reservoir analogs.
- 340 BOEM (2017), Northern GoM Deepwater Bathymetry Grid from 3D Seismic [Data file].  
341 Retrieved from [https://www.boem.gov/oil-gas-energy/mapping-and-data/map-](https://www.boem.gov/oil-gas-energy/mapping-and-data/map-gallery/northern-gom-deepwater-bathymetry-grid-3d-seismic)  
342 [gallery/northern-gom-deepwater-bathymetry-grid-3d-seismic](https://www.boem.gov/oil-gas-energy/mapping-and-data/map-gallery/northern-gom-deepwater-bathymetry-grid-3d-seismic).
- 343 Brunt, R. L., W. D. McCaffrey, and B. C. Kneller (2004), Experimental modeling of the spatial  
344 distribution of grain size developed in a fill-and-spill mini-basin setting, *Journal of Sedimentary*  
345 *Research*, 74(3), 438-446.
- 346 Carter, L., R. Gavey, P. J. Talling, and J. T. Liu (2014), Insights into submarine geohazards from  
347 breaks in subsea telecommunication cables, *Oceanography*, 27(2), 58-67.
- 348 Dubief, Y., and F. Delcayre (2000), On coherent-vortex identification in turbulence, *Journal of*  
349 *turbulence*, 1(1), 011.
- 350 Ellison, T., and J. Turner (1959), Turbulent entrainment in stratified flows, *Journal of Fluid*  
351 *Mechanics*, 6(3), 423-448.
- 352 Fukuda, S., M. G. de Vet, E. W. Skevington, E. Bastianon, R. Fernández, X. Wu, W. D. McCaffrey,  
353 H. Naruse, D. R. Parsons, and R. M. Dorrell (2023), Inadequacy of fluvial energetics for  
354 describing gravity current autosuspension, *Nature Communications*, 14(1), 2288.
- 355 Gilbert, G. K., and E. C. Murphy (1914), *The transportation of debris by running water*, US  
356 Government Printing Office.
- 357 Hage, S., V. Galy, M. Cartigny, S. Acikalin, M. Clare, D. Gröcke, R. Hilton, J. Hunt, D. Lintern, and  
358 C. McGhee (2020), Efficient preservation of young terrestrial organic carbon in sandy turbidity-  
359 current deposits, *Geology*, 48(9), 882-887.
- 360 Islam, M. A., and J. Imran (2010), Vertical structure of continuous release saline and turbidity  
361 currents, *Journal of Geophysical Research: Oceans*, 115(C8).
- 362 Khripounoff, A., A. Vangriesheim, N. Babonneau, P. Crassous, B. Dennielou, and B. Savoye  
363 (2003), Direct observation of intense turbidity current activity in the Zaire submarine valley at  
364 4000 m water depth, *Marine geology*, 194(3-4), 151-158.

365 Lamb, M. P., T. Hickson, J. G. Marr, B. Sheets, C. Paola, and G. Parker (2004), Surging versus  
366 continuous turbidity currents: flow dynamics and deposits in an experimental intraslope  
367 minibasin, *Journal of Sedimentary Research*, 74(1), 148-155.

368 Lamb, M. P., H. Toniolo, and G. Parker (2006), Trapping of sustained turbidity currents by  
369 intraslope minibasins, *Sedimentology*, 53, 147-160.

370 Maharaj, V. T. (2012), The effects of confining minibasin topography on turbidity current  
371 dynamics and deposit architecture.

372 Meiburg, E., S. Radhakrishnan, and M. Nasr-Azadani (2015), Modeling gravity and turbidity  
373 currents: computational approaches and challenges, *Applied Mechanics Reviews*, 67(4).

374 Mitchum Jr, R. M., P. R. Vail, and J. B. Sangree (1977), Seismic stratigraphy and global changes  
375 of sea level: Part 6. Stratigraphic interpretation of seismic reflection patterns in depositional  
376 sequences: Section 2. Application of seismic reflection configuration to stratigraphic  
377 interpretation.

378 Patacci, M., P. D. Haughton, and W. D. Mccaffrey (2015), Flow behavior of ponded turbidity  
379 currents, *Journal of Sedimentary Research*, 85(8), 885-902.

380 Pirmez, C., B. E. Prather, G. Mallarino, W. W. O'Hayer, A. W. Droxler, and C. D. Winker (2012),  
381 Chronostratigraphy of the Brazos-Trinity Depositional System, Western Gulf of Mexico:  
382 Implications for Deepwater Depositional Models, in *Application of the Principles of Seismic  
383 Geomorphology to Continental-Slope and Base-of-Slope Systems: Case Studies from Seafloor  
384 and Near-Seafloor Analogues*, edited by B. E. Prather, M. E. Deptuck, D. Mohrig, B. Van Hoorn  
385 and R. B. Wynn, pp. 111-143, SEPM.

386 Pohl, F., J. T. Eggenhuisen, M. Cartigny, M. Tilston, J. de Leeuw, and N. Hermidas (2020a), The  
387 influence of a slope break on turbidite deposits: an experimental investigation, *Marine Geology*,  
388 424, 106160.

389 Pohl, F., J. T. Eggenhuisen, I. A. Kane, and M. A. Clare (2020b), Transport and burial of  
390 microplastics in deep-marine sediments by turbidity currents, *Environmental science &  
391 technology*, 54(7), 4180-4189.

392 Prather, B. E., C. Pirmez, C. D. Winker, M. Deptuck, D. Mohrig, B. Van Hoorn, and R. Wynn  
393 (2012), Stratigraphy of linked intraslope basins: Brazos-Trinity system western Gulf of Mexico,  
394 *Application of the principles of seismic geomorphology to continental-slope and base-of-slope  
395 systems: Case studies from seafloor and near-seafloor analogues: SEPM, Special Publication*, 99,  
396 83-109.

397 Satterfield, W. M., and E. Behrens (1990), A late Quaternary canyon/channel system, northwest  
398 Gulf of Mexico continental slope, *Marine Geology*, 92(1-2), 51-67.

399 Sequeiros, O. E., B. Spinewine, R. T. Beaubouef, T. Sun, M. H. García, and G. Parker (2010),  
400 Characteristics of velocity and excess density profiles of saline underflows and turbidity  
401 currents flowing over a mobile bed, *Journal of Hydraulic Engineering*, 136(7), 412-433.

402 Soutter, E. L., D. Bell, Z. A. Cumberpatch, R. A. Ferguson, Y. T. Spsychala, I. A. Kane, and J. T.  
403 Eggenhuisen (2021), The influence of confining topography orientation on experimental  
404 turbidity currents and geological implications, *Frontiers in Earth Science*, 8, 540633.

405 Sparkes, R. B., I.-T. Lin, N. Hovius, A. Galy, J. T. Liu, X. Xu, and R. Yang (2015), Redistribution of  
406 multi-phase particulate organic carbon in a marine shelf and canyon system during an  
407 exceptional river flood: Effects of Typhoon Morakot on the Gaoping River–Canyon system,  
408 *Marine Geology*, 363, 191-201.

409 Spinewine, B., O. E. Sequeiros, M. H. Garcia, R. T. Beaubouef, T. Sun, B. Savoye, and G. Parker  
410 (2009), Experiments on wedge-shaped deep sea sedimentary deposits in minibasins and/or on  
411 channel levees emplaced by turbidity currents. Part II. Morphodynamic evolution of the wedge  
412 and of the associated bedforms, *Journal of Sedimentary Research*, 79(8), 608-628.  
413 Toniolo, H., M. Lamb, and G. Parker (2006a), Depositional turbidity currents in diapiric  
414 minibasins on the continental slope: formulation and theory, *Journal of Sedimentary Research*,  
415 76(5), 783-797.  
416 Toniolo, H., G. Parker, V. Voller, and R. Beaubouef (2006b), Depositional turbidity currents in  
417 diapiric minibasins on the continental slope: experiments—numerical simulation and upscaling,  
418 *Journal of Sedimentary Research*, 76(5), 798-818.  
419 Traer, M., A. Fildani, O. Fringer, T. McHargue, and G. Hilley (2018), Turbidity current dynamics:  
420 1. Model formulation and identification of flow equilibrium conditions resulting from flow  
421 stripping and overspill, *Journal of Geophysical Research: Earth Surface*, 123(3), 501-519.  
422 van Andel, T. H., and P. D. Komar (1969), Pondered sediments of the Mid-Atlantic Ridge between  
423 22 and 23 North latitude, *Geological Society of America Bulletin*, 80(7), 1163-1190.  
424 Violet, J., B. Sheets, L. Pratson, C. Paola, R. Beaubouef, and G. Parker (2005), Experiment on  
425 turbidity currents and their deposits in a model 3D subsiding minibasin, *Journal of Sedimentary  
426 Research*, 75(5), 820-843.  
427 Wang, X., S. M. Luthi, D. M. Hodgson, D. Sokoutis, E. Willingshofer, and R. M. Groenenberg  
428 (2017), Turbidite stacking patterns in salt-controlled minibasins: insights from integrated  
429 analogue models and numerical fluid flow simulations, *Sedimentology*, 64(2), 530-552.  
430 Winker, C. D. (1996), High-resolution seismic stratigraphy of a late Pleistocene submarine fan  
431 ponded by salt-withdrawal mini-basins on the Gulf of Mexico continental slope, paper  
432 presented at Offshore Technology Conference, OnePetro.  
433 Yang, S., Y. An, and Q. Liu (2019), A two-dimensional layer-averaged numerical model for  
434 turbidity currents, *Geological Society, London, Special Publications*, 477(1), 439-454.

435

436